nature communications

Article

https://doi.org/10.1038/s41467-025-57498-y

Irreproducible SEBS wrinkling based on spin evaporation enabling identifiable artificial finger pad electronics

Received: 16 January 2024

Accepted: 24 February 2025

Published online: 05 March 2025

Check for updates

Juyeong Lee[1,5], Haechan Park[1,5], Sehyun Kim[1], Chang Liu[2], Zhengwei Li[2,3] & Kyoseung Sim[1,4]

Irreproducible wrinkling, characterized by randomly arranged ridges or creases on material surfaces, has significant potential for application in entity identification and anti-counterfeiting. However, active research in this field is hindered because the existing wrinkling methods face challenges in realizing discernible patterns and potential applications of submillimeter-scale wavelength wrinkles are yet to be identified. Herein, we propose a strategy to create unique and irreproducible styrene–ethylene–butylene–styrene (SEBS) wrinkles using "spin evaporation", a technique that rapidly removes the solvent by spinning. We demonstrate the realization of SEBS wrinkles with wavelengths of hundreds of micrometers with high randomness, irreproducibility, and resistance to external stimuli. Importantly, to demonstrate the potential application of the wrinkle, we suggest and fabricate a human-finger-like fully soft identifiable artificial finger pad electronics and integrate it with a soft bimodal sensing system. The artificial finger pad mimics human finger pad features such as identification, object recognition, and effective grasping. Further integration of this pad into soft robots, cephalopods, and prosthetic skin offers insightful potential for the proposed wrinkling method in various fields.

The study of wrinkles—pervasive patterns observed in nature—contributes to substantial technical advancements in areas such as optical property modulation[1–4], wettability control[5,6], dynamic adhesion[7,8], and stretchable electronics[9]. In particular, irreproducible wrinkling, which generates unique arbitrary patterns each time, has attracted significant attention owing to its applications in entity identification and anti-counterfeiting (e.g., physical unclonable functions)[10–14]. Presently, the effective detection and authentication of patterns with a range of nano- to submicron-scale wrinkle wavelengths require high-cost, high-resolution, and complex systems[11,12]. Furthermore, the absence of a mechanically deformable feature in these patterns (capable of enduring external stimuli) restricts their applicability because their practical applications often subject these patterns to various external stimuli such as mechanical deformation and physical contact[15,16]. The significant challenges associated with creating discernible patterns with large-wavelength wrinkles (on the order of hundreds of micrometers) and ensuring their mechanical deformability remain unaddressed. The present situation is attributed to the inherent difficulty in achieving large-wavelength wrinkling with irreproducible patterns on elastomer surfaces and a lack of substantial applications that could spur intensive research in this field. Therefore, there is a need to develop an approach to creating sufficiently discernible random wrinkles with mechanically deformable features via a facile process, as well as identifying impactful applications for such wrinkle patterns.

Here, we propose an innovative strategy, termed "spin evaporation", to form discernible and irreproducible wrinkles on styrene-

[1]Department of Chemistry, Ulsan National Institute of Science and Technology (UNIST), Ulsan, Republic of Korea. [2]Department of Biomedical Engineering, University of Houston, Houston, TX, USA. [3]Department of Biomedical Sciences, University of Houston, Houston, TX, USA. [4]X-Dynamic Research Center, Ulsan National Institute of Science and Technology (UNIST), Ulsan, Republic of Korea. [5]These authors contributed equally: Juyeong Lee, Haechan Park.
e-mail: kyos@unist.ac.kr

ethylene-butylene-styrene (SEBS), featuring a mechanically soft nature with submillimeter-scale wavelength. This method is based on swift solvent removal through the horizontal spinning of a film, which is cost-effective and enables the formation of large-area, unique, irreproducible random patterns of SEBS wrinkles. Unlike conventional techniques, this approach utilizes spinning for solvent treatment only without an additional layer coating to form wrinkles.

The SEBS wrinkles obtained using this method exhibit a high degree of randomness and irreproducibility, demonstrating excellent authentication and identification properties. In addition, SEBS wrinkles exhibit high resistance to various external stimuli, including mechanical strain, abrasion, pressure, and environmental factors such as temperature and hydration. Moreover, we propose and demonstrate impactful applications of irreproducible SEBS wrinkles characterized by sufficiently discernible patterns. As a representative application of the proposed method, we fabricate a human-finger-like soft artificial finger pad using a fingerprint derived from SEBS wrinkle patterns and integrate it with a soft bimodal sensing system. The irreproducible pattern enhances security for identification and authentication in our artificial finger pad electronics, representing a significant departure from existing reports on finger pad electronics that utilize physical patterns for triboelectric tactile sensing[17,18], vibrotactile signal sensing[19], energy harvesting[20], and effective grasping[21]. More specific comparisons are summarized in Supplementary Table 1. Experimental results obtained using the fabricated device suggest the potential of the proposed method for critical real-world applications because the artificial finger pad successfully emulates human finger-like functions, including fingerprint authentication, object recognition, surface texture distinction, and effective object gripping. The expanded scope of the irreproducible SEBS wrinkles is further demonstrated, presenting a broad spectrum of potential applications across various fields, including in soft robotics, cephalopod-inspired devices, and prosthetic skin technologies.

Results

Irreversible SEBS wrinkle based identifiable artificial finger pad electronics

SEBS is a widely used triblock copolymer consisting of crystalline polystyrene and amorphous poly(ethylene-butylene) regions, as shown in Fig. 1a. It is a well-known elastomer with excellent mechanical stretchability, robustness, weather resistance, and biocompatibility. It is suitable for various applications such as wearable electronics, electronic skin, and other outdoor applications[22–24]. Figure 1b shows a schematic illustration of the proposed strategy for submillimeter-scale SEBS wrinkle formation through swift solvent removal using spin evaporation. The spin evaporation technique involves only a solvent treatment without any additional layer coating. Distinct from traditional evaporation methods that involve gradual solvent removal, this technique allows precise control over solvent retention time on the SEBS surface, achieved through rapid evaporation under horizontal spinning as needed. The exposure duration of SEBS to the solvent is critical for wrinkle morphology, and spin evaporation plays a pivotal role. The detailed optimization will be discussed later in this paper.

The irreproducible SEBS wrinkles obtained using the spin evaporation method feature irregularly grooved patterns on a submillimeter wavelength scale, as shown in Fig. 1c–e. These irreproducible, unique, discernible, and robust characteristics of SEBS wrinkles can be utilized in various practical fields, enabling the mimicry of natural functions, such as those served by fingerprints. Indeed, fingerprints are a representative physical feature of finger pads, which offer distinctive patterns that enable the identification of individuals. However, most studies have overlooked the unique identification feature of human fingerprints, and the development of human-like robots or androids has predominantly focused on appearance[25], movement[26–29], and skin-like electronics[30–32]. Therefore, we demonstrate identifiable artificial finger pad electronics as an impactful application of irreproducible SEBS wrinkles, as shown in Fig. 1f. This artificial finger pad exhibited physical, functional, and mechanical attributes analogous to those of a human finger pad.

Discernible SEBS wrinkling by spin evaporation

The SEBS wrinkles were spontaneously formed on a UV-O_3 treated SEBS surface through solvent-induced swelling with spin evaporation. The process involves dropping toluene onto the SEBS film, followed by the rapid removal of toluene from the film via horizontal spinning, as schematically depicted in Fig. 2a. In particular, the surface of the SEBS film was exposed to UV-O_3 to induce cross-linking of molecular chains via radical recombination[33,34]. The plausible cross-linking mechanism is proposed in Supplementary Fig. 1. The exposure to UV-O_3 generates diverse radicals, including alkyl, alkoxy, and peroxy radicals, within the aliphatic backbone of SEBS. These radicals can be randomly cross-linked, and some of the generated radicals can further form alcohols, aldehydes, ketones, acetophenones, and ester compounds[35]. The attenuated total reflection Fourier transformation infrared (ATR-FTIR) spectra of the UV-O_3 exposed SEBS film exhibited reduced sp^3 C − H absorption (2925 cm^{-1} and 2850 cm^{-1}) and enhanced O − H (3670–3000 cm^{-1}), C = O (1715 cm^{-1}), and C − O (1180 cm^{-1}) absorption with longer exposure times (Supplementary Fig. 2). These results confirm the cross-linking of SEBS upon UV-O_3 exposure. Although UV-O_3 treatment simultaneously induces chain scission and cross-linking in SEBS, gel permeation chromatography (GPC) results (Supplementary Fig. 3) indicate that 20 min of treatment led to an increase in the weight-average molecular weight (M_W) and polydispersity index, suggesting that cross-linking predominates over chain scission[36]. When toluene was applied to the UV-O_3 treated SEBS film, the cross-linked surface swelled. Consequently, the omnidirectionally expanded surface experienced self-generated in-plane compressive stress during toluene evaporation without any externally applied load, leading to wrinkling of the SEBS surface with irregularly shaped grooves, suitable for use as artificial fingerprints (Fig. 2b).

One critical aspect of the formation of wrinkles is plastic deformation caused by the swelling of the UV-O_3 treated SEBS surface. The swelling of the SEBS surface involves an irreversible expansion of the surface, preventing it from shrinking after deswelling, as shown in Supplementary Fig. 4. In this process, the irregularly shaped, grooved features of the pattern result from the stochastically varied mechanical properties of the cross-linked SEBS. Indeed, atomic force microscopy (AFM) images of the surface in the phase mode clearly exhibit stochastically altered mechanical properties of the SEBS surface through UV-O_3 induced cross-linking (Supplementary Fig. 5). To investigate the effect of such spatial variations in local stiffness on wrinkle configuration, finite element analysis (FEA) was performed, and the detailed simulation steps and results are described in Supplementary Note 1. As shown in Supplementary Fig. 6, the 2D FEA results clearly demonstrate that even minor, randomly distributed spatial variations in local stiffness can significantly change the final wrinkle pattern, thereby elucidating the origin of the irreproducible wrinkling. Furthermore, the 3D FEA results highlight the role of strain anisotropy during wrinkle formation, which significantly affects the morphology of the patterns generated in this study, as shown in Supplementary Figs. 7 and 8. These variabilities aligned with classical buckling theories, which highlight the sensitivity of wrinkle formation to material imperfections and applied strain[37]. Consequently, the combined effects of stochastic cross-linking and strain anisotropy preclude the formation of standardized or reproducible wrinkle morphologies, even under consistent processing conditions. In addition, the degree of cross-linking, determined by the UV-O_3 treatment time, affected the morphology of SEBS wrinkles. As shown in Supplementary Fig. 9, 20 min of UV-O_3 treatment resulted in the desired surface

https://doi.org/10.1038/s41467-025-57498-y

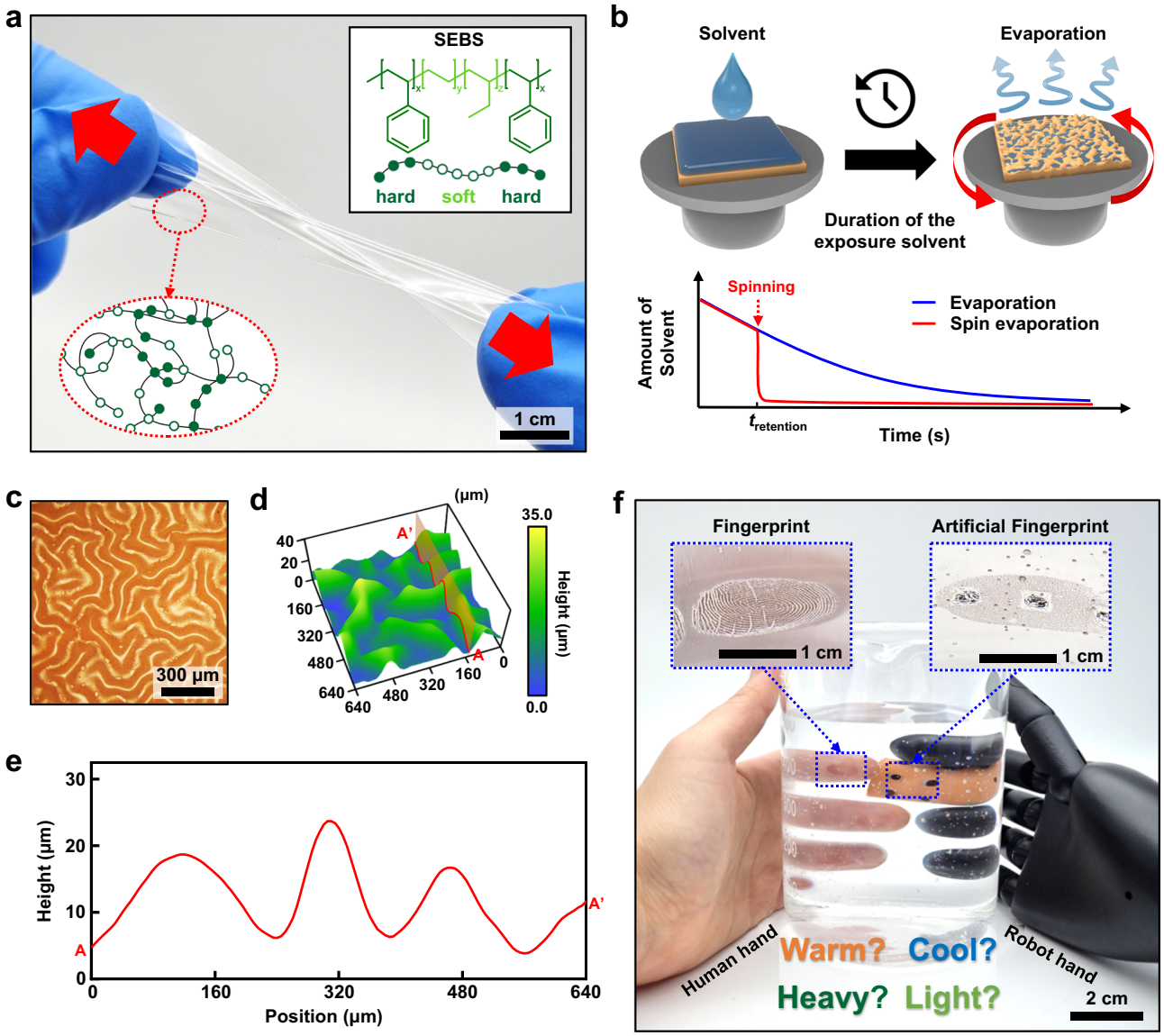

Fig. 1 | SEBS wrinkling enabling identifiable artificial finger pad electronics. **a** Optical image and schematic of SEBS structure. **b** Schematic of spin evaporation. **c**–**e** Representative optical microscopy (**c**), confocal laser scan microscopy (**d**), and cross-sectional profile (**e**) of SEBS wrinkle. **f** Optical image of the human hand and identifiable artificial finger pad electronics.

morphology with irregularly corrugated patterns of the SEBS film. In contrast, insufficient or excessive cross-linking led to non-uniform wrinkling.

Another crucial aspect is spin evaporation, which results in a rapid removal of the solvent toluene. Solvent removal was achieved by spinning the UV-O_3 treated SEBS surface immediately after toluene was dropped onto it. Otherwise, toluene would penetrate the film and dissolve an excessive number of SEBS molecules beneath the cross-linked surface, resulting in non-uniform wrinkling, as shown in Supplementary Fig. 10. It should be noted that applying high temperatures for faster solvent evaporation resulted in non-uniform wrinkling owing to accelerated dissolution (Supplementary Fig. 11). To determine the appropriate time for a desired pattern, the retention time of the solvent on the UV-O_3 treated SEBS was optimized. In this study, 5 s was found to be the most appropriate (Supplementary Fig. 12). In addition, the solubility of SEBS in the solvent used for spin evaporation is another crucial factor for appropriate wrinkle formation. As shown in Supplementary Fig. 13 and Supplementary Table 2, solvents that have low solubility in SEBS cannot induce wrinkles due to their inability to swell the cross-linked SEBS surface. The specific conditions for the reliable formation of discernible wrinkles were systematically optimized, enabling a randomly featured patterned topography across a large area of the SEBS film, as shown in Fig. 2c and Supplementary Fig. 14. The SEBS film exhibits a maximum dimension of up to 7.5 cm × 5.0 cm, with high pattern coverage and continuity (Supplementary Fig. 15).

Human fingerprints are exposed to various environmental stimuli such as mechanical deformation, moisture, and heat in daily life. Therefore, ensuring the physical stability of the pattern of an artificial fingerprint is essential for its utilization in artificial finger pads. Figure 2d depicts representative optical microscopy images of an artificial fingerprint before and after being subjected to various external stimuli, including a strain of 30%, thermal stress at approximately 90 °C for 24 h, moisture by soaking in tap water for 24 h, abrasion caused by mechanical rubbing with a stainless steel stick for 300 times, and pressure applied by pressing with a 100 g weight. The durability of the patterns against external stimuli is demonstrated by comparing the wavelength and amplitude extracted from confocal laser scanning

https://doi.org/10.1038/s41467-025-57498-y

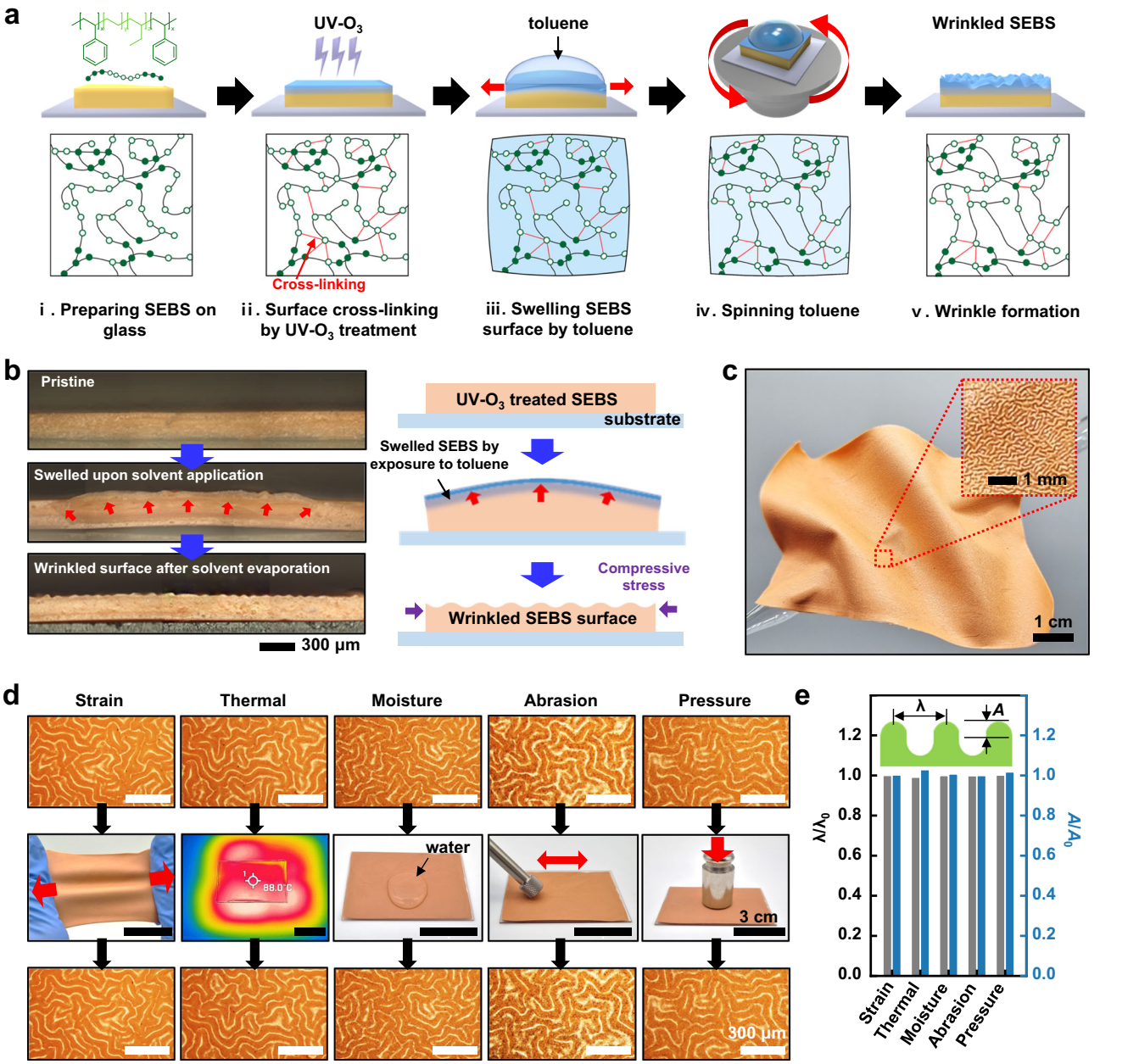

Fig. 2 | Discernible SEBS wrinkling by spin evaporation. a Schematic of the wrinkle formation process. **b** Optical microscopy images (left) and schematic cross-sectional illustration (right) of sequential wrinkle formation process. **c** Optical image of artificial fingerprint in a large area. **d** Optical images and optical microscopy images of artificial fingerprints before (top), during (middle), and after (bottom) exposure to various stimuli. **e** Changes in wavelength (λ/λ_0) and amplitude (A/A_0) of wrinkles under various stimuli.

microscopy images (Supplementary Fig. 16). As shown in Fig. 2d, e and Supplementary Fig. 17, the artificial fingerprint exhibited excellent physical durability against these external stimuli. Furthermore, the artificial fingerprint featured not only mechanical endurance of harsh stimuli, including cyclic strain, static strain, and low temperatures down to − 20 °C (Supplementary Fig. 18), but also chemical resistance to various conditions such as PBS, acetone, ethanol, acid, and base, and human sweat (Supplementary Fig. 19). These results clearly indicate that the artificial fingerprint used in this study can be utilized effectively as identifiable artificial finger pad electronics.

Authentication property of irreproducible SEBS wrinkle

The irregular patterns of irreproducible SEBS wrinkles enable the assignment of a unique identifier to individual objects such as androids, thereby facilitating their tracking, maintenance, and management throughout their lifecycle after registration and authentication. Hence, the uniqueness of the SEBS wrinkle pattern was evaluated in this study to validate its potential suitability as an identifier, such as a fingerprint. The optical microscopy images of wrinkles were converted into binary images using Otsu's algorithm, as shown in Fig. 3a. This image-processing technique determines the optimal threshold value by analyzing the image histogram (Supplementary Fig. 20). As a proof-of-concept, authentication was demonstrated by comparing binarized optical microscopy images of wrinkles using Python with Oriented Fast and Rotated BRIEF (ORB) and Brute-Force Matcher (BFMatcher) algorithms (Supplementary Note 2). The comparison results can be quantified into a specific value that represents the degree of similarity between images. A cross-correlation analysis of 70 wrinkles (Supplementary Fig. 21) was performed using the image comparison method described above. The heatmap (Fig. 3b) and

https://doi.org/10.1038/s41467-025-57498-y

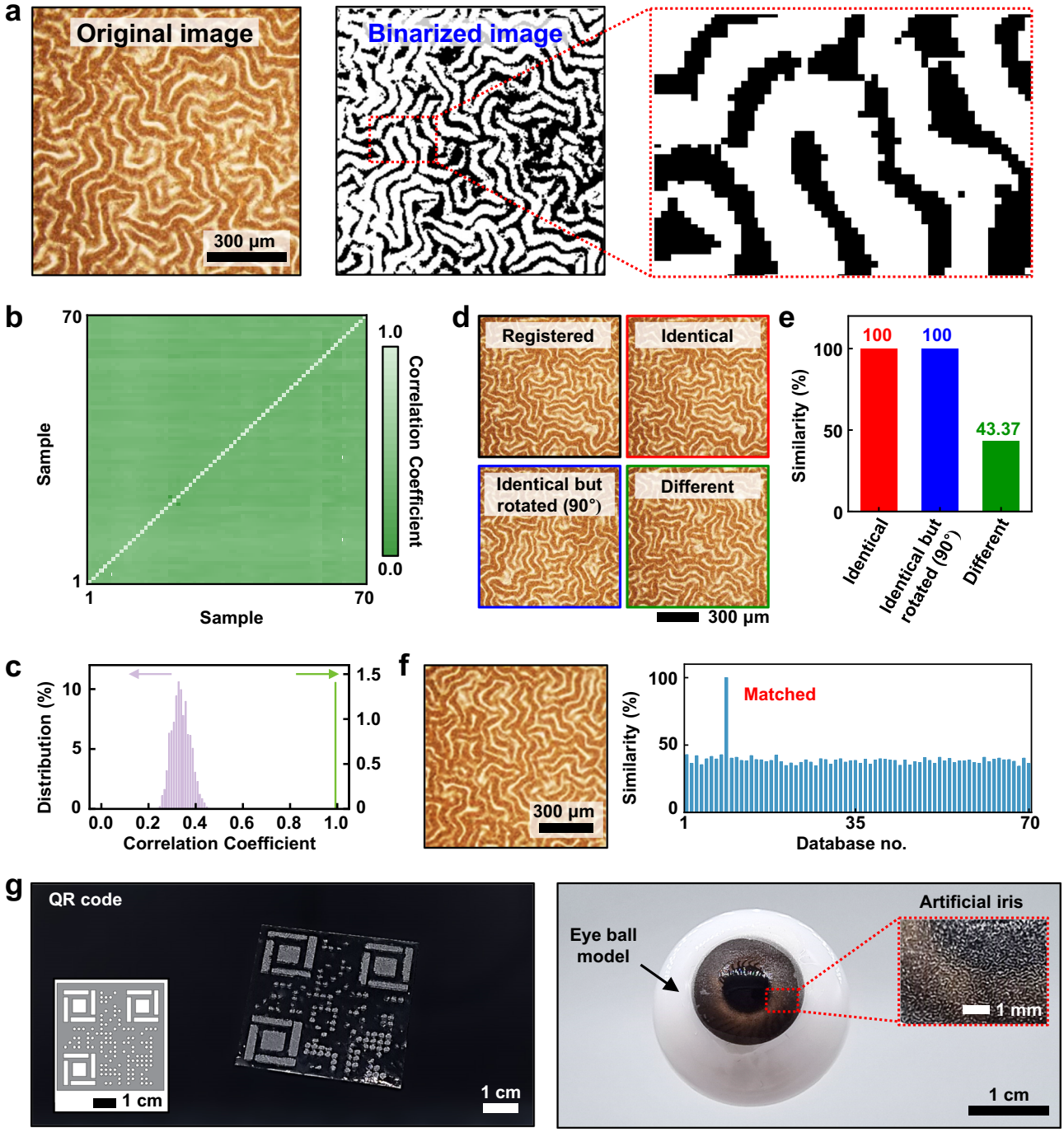

Fig. 3 | Authentication using SEBS wrinkle pattern. a Optical microscopy image (left), the binarized image of the wrinkle (middle), and a magnified binarized image (right). **b** Cross-correlation map of the database with 70 different wrinkles. **c** Distribution of cross-correlation values of the database. **d** Optical microscopy images of specific wrinkles for authentication test. **e** Authentication results of the prepared optical microscopy images of wrinkles. **f** Optical microscopy image of a specific wrinkle from the database (left) and identification result of that image from the database (right). **g** Further applications of random wrinkles utilized in highly secured QR codes (left) and artificial irises (right) (Inset on the left image presents the design of the QR code).

histograms (Fig. 3c) of the cross-correlation analysis results exhibited excellent authentication and identification features, returning a high correlation coefficient (i.e., similarity) of near unity for identical images and a low value of less than 0.45 for different images. In addition, a practical example of authentication was demonstrated by comparing three images: one image was identical to the registered image, another was identical but rotated by 90°, and the third image was distinctly different (Fig. 3d). As shown in Fig. 3e, excellent authentication capacity was demonstrated by a 100% similarity value for both identical and rotated images with reference to the registered image, whereas the different image showed a similarity of less than 50%. The identification capability is further demonstrated in Fig. 3f, which shows an excellent discernible function among the 70 pre-registered patterns (Supplementary Fig. 21). A mathematical model incorporating combinatorial calculations to quantify the irreproducibility of SEBS wrinkle patterns reveals that the probability of generating two identical patterns within a 1 mm × 1 mm sample is nearly one in 10^{43}. The detailed calculations supporting this estimation are provided in Supplementary Note 3.

Because SEBS wrinkles primarily depend on the UV-O_3 treatment, custom-designed conventional patterns containing irregularly

corrugated sub-patterns can be created using a selective UV-O_3 exposure using a shadow mask (Supplementary Fig. 22). Supplementary Fig. 23 shows representative demonstrations of various patterns containing wrinkled configurations successfully fabricated as desired. Consistent with our earlier simulations, the FEA results for these patterned samples confirm significant strain anisotropy during the wrinkling process, as shown in Supplementary Fig. 24, further validating the role of anisotropic strain in wrinkling. Owing to the significant advantages of the facile wrinkle formation process for customizable designs, this approach can be applied to various fields such as QR codes and artificial irises, as shown in Fig. 3g. These examples highlight the significant security enhancements that could be achieved through our approach, specifically by using QR codes with irreproducible random sub-patterns and artificial irises with unique wrinkling patterns imitating human irises (Supplementary Note 4). The potential for applications of this method in high-level security and the development of more human-like androids highlight the significance of this study.

Identifiable artificial soft finger pad electronics

Fingerprints feature unique patterns for individual identification. The proliferation of humanoid robots, especially androids that mimic human traits, has aided various fields[38–41]. Although advancements have been made in motion[26–29], artificial intelligence[42,43], and human-like appearance[25], artificial fingers remain underexplored despite their significance. Integrating fingerprint technology in androids offers unique and secure identities, enhancing security and interaction authenticity in the Internet of Things systems as well as enabling effective tracking and maintenance throughout their lifecycle.

Figure 4a depicts an optical image of a robotic hand incorporating identifiable artificial finger pad electronics in a fully soft format that consists of fingerprint-inspired identifiable patterns and soft electronics with bimodal sensing capabilities. The pattern features an irregular groove formed by the wrinkling of SEBS in unpredictable shapes, which impart a unique, recognizable, distinguishable, and identifiable character to a particular entity. Such patterns can be considered artificial fingerprints. In addition, the bimodal sensing soft electronics, comprising resistive temperature sensors based on organic semiconductors and capacitive pressure sensors based on porous elastomers, enable simultaneous and discriminating temperature and pressure monitoring. The artificial finger pad was fabricated as a vertical assembly of a temperature-sensor-embedded artificial fingerprint and porous elastomer-based pressure sensor as schematically illustrated in Fig. 4b. Soft and thin polydimethylsiloxane (PDMS) (with a monomer-to-cross-linker ratio of 20:1) was used as an adhesive between the components (Supplementary Fig. 25) to ensure the softness of the artificial finger pad. A soft temperature sensor was fabricated using a composite of poly(3-hexylthiophene) nanofibrils, PDMS (P3HT-NFs/PDMS), and silver nanowires (AgNWs) embedded in SEBS (AgNWs/SEBS). A soft pressure sensor was fabricated using porous PDMS and AgNWs embedded in PDMS (AgNWs/PDMS) electrodes assembled in a sandwich structure. A cross-sectional image and schematic of the device are shown in Supplementary Fig. 26. The detailed features and fabrication processes of all components are described later.

As mentioned previously, the softness of the artificial fingerprint, along with the temperature and pressure sensors, must be adequate to mimic the various functionalities of the human finger pad. Figure 4c presents the stress-strain curves of each component used to fabricate the soft and identifiable artificial finger pad electronics. The Young's moduli of wrinkled SEBS, AgNWs/SEBS, porous PDMS, and AgNWs/PDMS were obtained as 3.01 MPa, 1.46 MPa, 95.9 kPa, and 2.69 MPa, respectively, with corresponding fracture strains of 958.8%, 744.8%, 80.87%, and 109.0%. Although these moduli are relatively higher than those of the human finger pad (between 0.07 MPa and 0.2 MPa)[44], they are sufficiently soft to be used as artificial finger pad[45,46]. Figure 4d shows various mechanical deformations, such as bending, stretching, and poking, of the artificial finger pad electronics. Owing to the soft character of all the components used in the fabrication of the artificial finger pad, the pad can be deformed without any physical damage.

Under real-world conditions, the human finger can sense multiple stimuli, which assists in compensating for the limitation of visual perception. Therefore, the artificial finger pad must be compatible with various sensing modes to closely mimic the functions of the natural finger. Particularly, sensing temperature and pressure using the finger is invaluable in enabling humans to recognize objects. In this study, we fabricated a fully soft bimodal sensor capable of discriminating between temperature and pressure detection. This was achieved via vertical integration of two components: a resistive temperature sensor (AgNWs/SEBS and P3HT-NFs/PDMS) and a capacitive pressure sensor (AgNWs/PDMS and porous PDMS). An organic semiconductor-based thermistor was adopted as the soft temperature sensor owing to its high sensitivity at low-temperature ranges, mechanical endurance, and simple fabrication process[32,47,48]. The temperature sensor was fabricated with a two-terminal planar configuration using AgNWs/SEBS and P3HT-NFs/PDMS as soft electrodes and soft temperature-sensing components, respectively. The fabrication process of the temperature sensor is schematically illustrated in Supplementary Fig. 27 and is described in the Methods. Supplementary Fig. 28a shows resistance changes of the sensor upon a temperature range from 20 °C to 50 °C, which presents typical thermistor behavior with a negative temperature coefficient (NTC)[47]. The linearly fitted natural logarithm of resistance ($\ln R$) versus the reciprocal of absolute temperature ($1/T$) was used to obtain the β parameter and temperature coefficient (α) (Supplementary Fig. 28b). The detailed calculations for extracting these values are provided in Supplementary Note 5. Supplementary Fig. 29 shows the continuous temperature-monitoring results of the soft sensor. These results are comparable to those of previously reported soft temperature sensors (Supplementary Table 3 and Supplementary Fig. 30). The relative resistance changes (Fig. 4e) and the extracted β parameter and α under the tensile strain of 30% (Supplementary Figs. 31 and 32) showed no significant degradation. Thus, the temperature sensor provides a reliable sensing capability under the typical deformation experienced by a human finger in everyday routine. Moreover, the effect of pressure on the soft-temperature sensor was investigated. Supplementary Fig. 33 shows a negligible resistance variation at 20 °C when applying a pressure of 0.56 kPa to the sensor. The fully soft nature of the temperature sensor alleviated the strain upon applying pressure, enabling the sensor to distinguish temperature information from another stimulus, pressure.

The capacitive pressure sensor was designed with a conventional sandwich structure comprising AgNWs/PDMS, porous PDMS, and AgNWs/PDMS as the bottom electrode, sensing layer, and top electrode, respectively. The remarkable mechanical endurance of the AgNWs/PDMS electrode features stable electrical conductivity under mechanical strain[49]. The pressure sensor measures the changes in capacitance caused by the application of pressure on the sensor, and the sensing mechanism is described in Supplementary Note 6. The details of the fabrication process are schematically illustrated in Supplementary Fig. 34 and are described in the Methods. Porous PDMS was chosen owing to its benefits, such as simple preparation, excellent softness, relatively high sensitivity, and high thermal resistance[50–52]. Considering the ease, low cost, and eco-friendliness of the process, manually pressed sugar was used to prepare a template for forming porous PDMS. The schematics of the porous PDMS preparation are depicted in Supplementary Figs. 35–37 and described in the Methods. Figure 4f shows the representative capacitance change in the pressure sensor plotted as a function of pressure change from 0 to 20 kPa, which corresponds to the typical pressure experienced by the human finger when touching or holding objects. The sensor exhibits a linear

https://doi.org/10.1038/s41467-025-57498-y

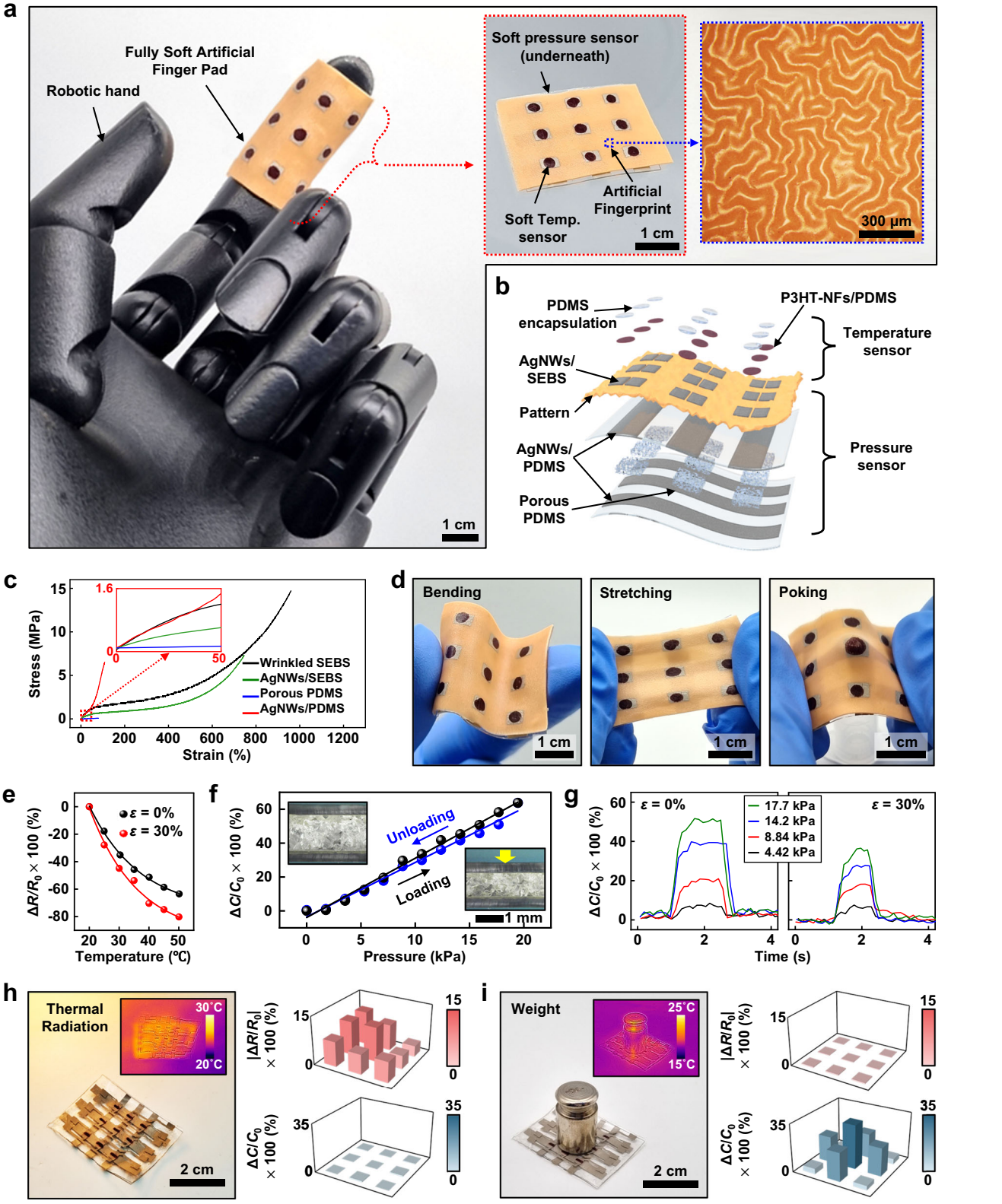

Fig. 4 | Soft artificial finger pad. a Optical images of the soft artificial finger pad on robotic hand (left), freestanding artificial finger pad (middle), and optical microscopy image of artificial fingerprint (right). **b** Schematic exploded view of the fully soft artificial finger pad. **c** Stress-strain curves of components used. **d** Optical images of artificial finger pads under various mechanical deformations. **e** Relative resistance change (R/R_0) in soft temperature sensors under the tensile strain of 0% and 30%. **f** Calibration curves of soft pressure sensor under loading and unloading (Inset is optical cross-sectional images of pressure sensor). **g** Responses of soft pressure sensor for various pressures under the tensile strain of 0% and 30%. **h**, **i** Spatial mapping of temperature and pressure distributions obtained using the soft bimodal sensor under thermal stimulus (**h**) and pressure (**i**). (Inset is the infrared images depicting temperature distribution).

response with sensitivities ($S = (\Delta C/C_0)/\Delta P$) of 3.498%/kPa and 3.214%/kPa under loading and unloading, respectively. It is noted that the thickness of the porous PDMS was fixed at 1.0 mm to ensure a sufficiently thin profile and enhance the wearability of the device. Supplementary Fig. 38 shows the capacitance profiles with clear dynamic responses under various pressures. No obvious degradation is observed under repeated cycling loading/unloading tests after 100 cycles, as shown in Supplementary Fig. 39.

Owing to the soft character of all the components, the pressure sensor displayed normal sensing characteristics under a mechanical strain of 30%, as shown in Fig. 4g and Supplementary Fig. 40. A slight decrease in its sensitivity (2.108%/kPa during loading and 2.094%/kPa during unloading) was observed under a tensile strain of 30%. This decrease in sensitivity can be attributed to the thinning of the sensing layer caused by tensile strain. This condition requires a greater force to achieve an equivalent degree of thickness reduction (Supplementary Fig. 41). Considering the potential uses of the artificial finger pad, the soft nature of the pressure sensor is more critical than maintaining a consistent value under high strain. This is because the skin on the human finger pad experiences only slight stretching during normal daily activities[53]. Importantly, the capacitive pressure sensor exhibits temperature-insensitive characteristics at pressures of 0 kPa, 4.42 kPa, and 17.7 kPa, as shown in Supplementary Fig. 42. This is a well-known advantage reported previously elsewhere as well[54,55]. The pressure-sensing capability, independent of temperature change, enables the sensor to accurately monitor pressure in situations where various stimuli are mixed, similar to real environments.

Spatial mapping results were obtained from a soft bimodal sensor array (3 × 3). Figure 4h shows the sensor array under thermal radiation, demonstrating distinct temperature mapping without detecting any signal from the pressure-sensing component. When a 50 g weight was loaded onto the soft bimodal sensor array, the pressure distribution was successfully mapped without faulty temperature recognition owing to signal interference, as shown in Fig. 4i. This result demonstrates the effectiveness of the fully soft bimodal sensor for accurately detecting and differentiating pressure and temperature stimuli, making it a promising solution for developing more realistic artificial finger pads.

Application of identifiable artificial finger pad electronics

Identifiable artificial finger pad electronics, composed of a randomly wrinkled pattern and a bimodal sensor, feature physical uniqueness, discriminated sensing, and mechanical softness. These advantages can enable robotic fingers equipped with artificial finger pads to act as substitutes for biological fingers[56–58]. Figure 5a shows two robotic hands with distinctly identifiable artificial finger pad electronics. Because of the unpredictably shaped wrinkles on the finger pad, the pattern can be used as an identification marker for each robotic hand, similar to a human fingerprint. Practically, distinct patterns of artificial fingerprints can be detected and successfully identified using inexpensive commercially available systems. The pattern features of the artificial fingerprints were further optimized, as depicted in Supplementary Fig. 43, to enhance recognition using a commercial scanner (Supplementary Fig. 44). Figure 5b depicts the process of artificial fingerprint authentication using a commercially available fingerprint scanner. Importantly, even a portion of the registered pattern could be verified as a match, whereas a different image did not yield a match. The authentication system is shown in Supplementary Fig. 45, and the detailed process is described in Supplementary Note 7.

By utilizing a bimodal sensor, the robotic finger could distinguish objects based on the simultaneous sensing of both temperature and pressure. Figure 5c demonstrates the recognition capability of the identifiable artificial finger pad electronics for representative objects featuring various temperatures and hardness: an LED bulb (hard and warm (40.6 °C)), a drink can (hard and cool (19.8 °C)), an orange (soft and cool (17.7 °C)), and human skin (soft and warm (31.7 °C)). The temperature and pressure profiles for the recognition of these objects were obtained from the calibration curves of the bimodal sensor, as shown in Supplementary Fig. 46. Note that the artificial fingerprint did not affect the morphology or properties of the AgNWs/SEBS electrode (Supplementary Fig. 47). Upon contact between the artificial finger pad of the robotic hand and various objects, the capability to detect temperature and pressure simultaneously and independently enabled the robotic hand to recognize living creatures characterized by their soft and warm traits, and distinguish them from various artificial objects. Further enhancement of the pressure sensor properties, which enables precise classification of soft, medium, and hard touches, can be achieved by optimizing the active layer through a multilayered architecture and incorporating nanomaterials. Consequently, it can be used in various fields, such as preventing unexpected accidents caused by undesired contact in industrial settings where humans and robots coexist.

The ridge-like configuration of the fingerprint on the identifiable artificial finger pad electronics facilitated the perception of textured surfaces. When a wrinkled artificial finger pad made contact with an uneven surface, it created a unique pattern of localized contact points. Such distinct contacts entail intensified physical resistance during mechanical rubbing, generating friction-induced vibrations. As the sensor sweeps across various textured surfaces, such as stainless steel and cork (Supplementary Fig. 48), dynamic variations in the effective contact area produce distinct traces in the measured pressure signals (Fig. 5d). These results clearly demonstrate the human-finger-like capability of the identifiable artificial finger pad electronics to recognize distinctive surface textures. In addition, owing to its softness, the identifiable artificial finger pad electronics integrated on the robotic hand enhanced the gripping properties by conformal deformation, increasing the contact area compared with that of a rigid finger pad, as shown in Fig. 5e.

We further demonstrated a variety of applications for the proposed device and SEBS wrinkles (Fig. 5f). The identifiable artificial finger pad electronics can be integrated into soft robots, providing them with unique identification and sensing capabilities. The soft random patterns can be used to identify wildlife for research, conservation, and management purposes[59–61]. In particular, the highly soft character of these patterns can serve as an excellent identifier for soft organisms, such as mollusks, because of the conformal deformation of the pattern, which adapts to undulating movements without the discomfort associated with traditional rigid identifiers. Furthermore, this method can be used to create artificial fingerprints for humans, enhancing security through transplants in cases where the original fingerprint information has been compromised and improving the quality of life of individuals with severely damaged fingerprints owing to accidents or diseases. Although the additional applications demonstrated in this study still have some way to go, the proposed method has promising potential applications in various fields of science and engineering.

Identifiable adaptive soft robotic system

An adaptive soft robot with a unique identifier was further demonstrated. Adaptability, a critical feature in living organisms, is also crucial for soft robots. While many efforts are underway to develop adaptive soft robots[28,29], tracking technology for individual soft robots is essential for effective management[62]. Our identifiable artificial finger pad electronics provide adaptive functions for soft robots and facilitate individual tracking for efficient management, both enabled by their advanced sensing functions, identification capability, mechanical softness, and robust resistance to external stimuli.

Figure 6a shows a group of identifiable adaptive soft robots made of Ecoflex 00-30, with the details of the robot design and dimensions

https://doi.org/10.1038/s41467-025-57498-y

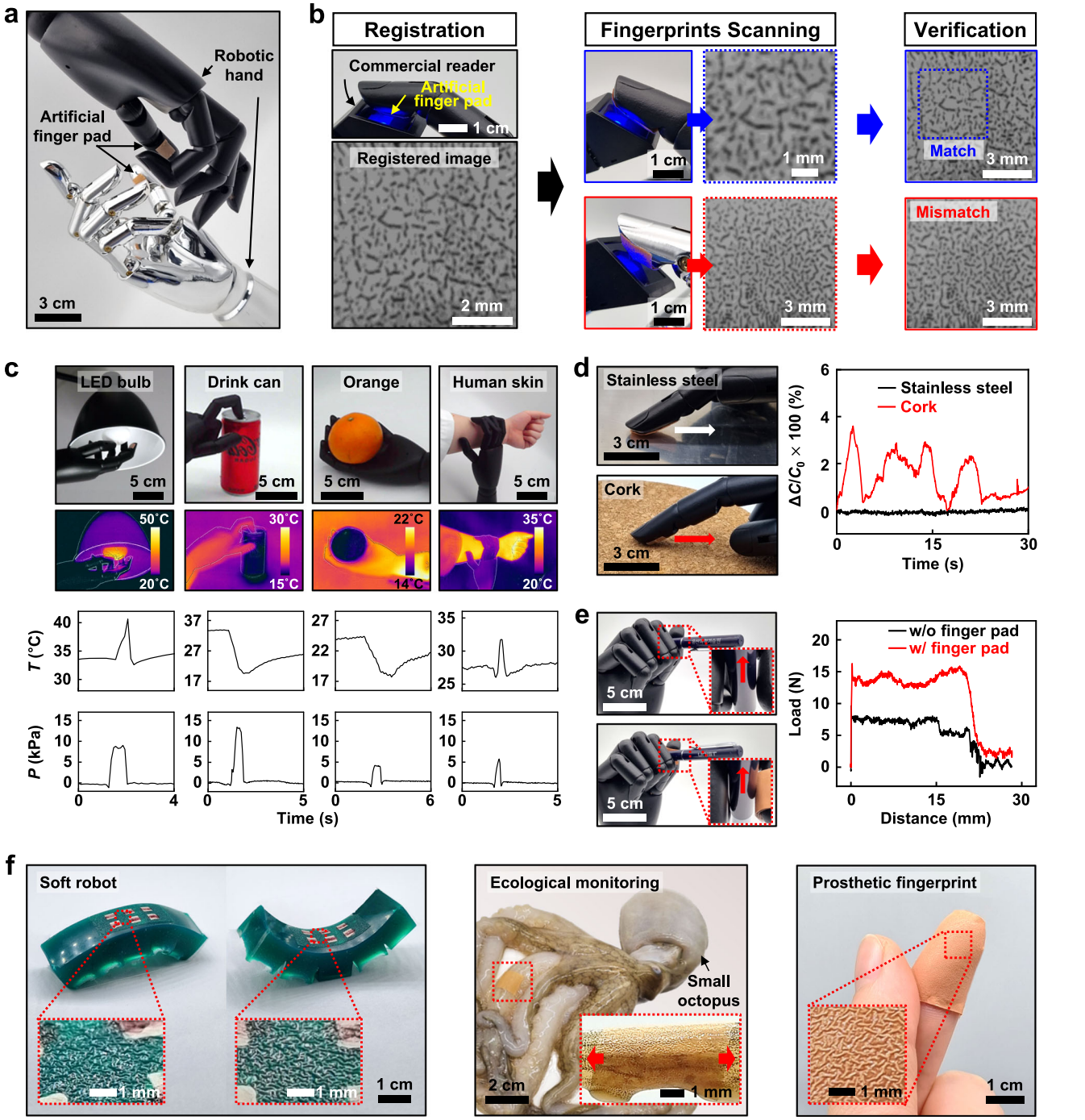

Fig. 5 | Applications of soft artificial finger pad. a Optical image of two distinct robotic hands, each equipped with its own unique artificial finger pad. **b** Process for authenticating identifiable robotic hands using the commercial fingerprint scanner. **c** Optical (top), IR images (middle), and output profile (bottom) of simultaneous sensing using an artificial soft finger pad. **d** Optical images (left) and capacitance change (right) in the texture perception during sweeps of artificial fingerprints on stainless steel and cork. **e** Optical images (left) and gripping properties (right) with and without the finger pad. **f** Diverse applications of soft artificial finger pads for identifiable soft robots (left), ecological monitoring (middle), and prosthetic fingerprints (right).

presented in Supplementary Fig. 49. These robots are equipped with soft temperature sensors for adaptive responses and SEBS-based identifiers, allowing distinct identification despite their identical appearance from mass production. The identifiable adaptive soft robot is pneumatically actuated (Fig. 6b) using an Arduino Uno, which controls both the air pump and the solenoid valve through a motor driver to regulate airflow and actuate the robot. The soft temperature sensor provides environmental temperature data to the Arduino Uno, allowing for adaptive control of the robot's movements. Figure 6c shows the block diagram of the system, with detailed interfaces in Supplementary Figs. 50 and 51. The locomotion of the robot is enabled by the bending of its body through pneumatic inflation, with anchor-pull by the front leg, followed by deflation of the body causing anchor-push by the rear leg, as shown in Supplementary Fig. 52. Upon detecting environmental changes, such as the approach of a hot object, the robot halts to avoid damage and resumes movement once the hazard is removed (Fig. 6d and Supplementary Fig. 53). These sequential processes clearly demonstrate its adaptive response to the

https://doi.org/10.1038/s41467-025-57498-y

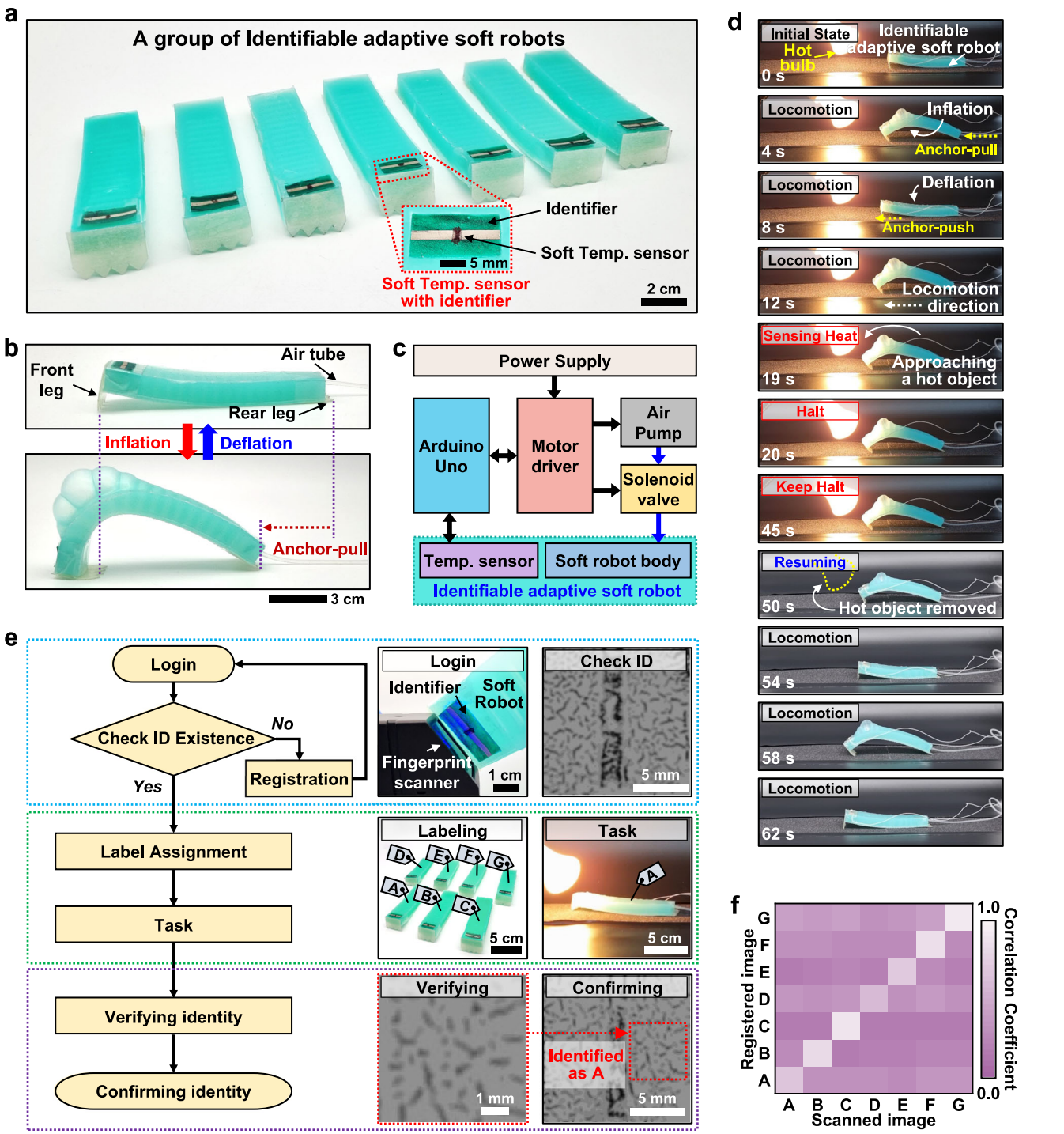

Fig. 6 | Identifiable adaptive soft robotic system. a Optical image of a group of identifiable adaptive soft robots. **b** Optical images of the pneumatic actuation process of the soft robot. **c** Block diagram of the identifiable adaptive soft robot system. Black and blue lines denote electrical and pneumatic connections, respectively. **d** Sequential images of the adaptive function of the soft robot. **e** Flowchart of managing and identifying the identifiable adaptive soft robotic system. **f** Cross-correlation coefficient map of the identifier of the identifiable adaptive soft robots.

environment. The detailed control mechanisms and code are described in Supplementary Note 8.

The unique identifier of the adaptive soft robot facilitates lifecycle management by enabling individual tracking and experience logging for each unit produced through mass production. As a representative example, Fig. 6e presents a flowchart designed for managing and identifying adaptive soft robots within a system. Initially, a manufactured identifiable adaptive soft robot is scanned for login using a commercial fingerprint scanner, followed by verification of registration status. Registered robots proceed to label assignments for tracking, while unregistered ones transition to registration. Once tracking begins, the robot embarks on its tasks, encountering various experiences such as approaching a hot object. For management purposes, the robot can be identified by scanning its unique identifier, allowing precise distinction among identical robots and tracking specific tasks performed or experiences encountered. The cross-correlation coefficient map of identifiable adaptive soft robots exhibits excellent identification capability,

enabling effective management (Fig. 6f). The system-level demonstration of the unique identifier and soft sensor integrated into the soft robot, enabling tracking and adaptability, highlights the practical potential of our approach.

Discussion

In conclusion, we proposed spin evaporation as a novel method to create SEBS wrinkles at a submillimeter wavelength scale and demonstrated its promising application for fabricating identifiable artificial finger pad electronics that mimics the physical, functional, and mechanical properties of the human finger pad. The SEBS wrinkles generated by spin evaporation were characterized by their substantial irreproducibility and randomness, exhibiting excellent authentication and identification characteristics and robust resistance to external stimuli. The demonstrated finger pad electronics uniquely identified and sensed both temperature and pressure, akin to a human finger. Further practical applications were demonstrated for fingerprint authentication, object recognition, texture distinction, and object gripping. Moreover, the soft and unique patterns suggest applications in wildlife identification, security systems, and prosthetics. This facile approach to creating SEBS wrinkles has a broad spectrum of potential applications, from advanced soft robotic systems to ecological research, thereby furthering research into large-wavelength wrinkles and their multifaceted utilities. Furthermore, system-level demonstrations of the identifiable adaptive soft robot underscore the practical effectiveness of our study. This spin evaporation technique can be a promising candidate for diverse materials-focused research necessitating solvent treatment.

Methods

Materials

Polystyrene-block-poly(ethylene-ran-butylene)-block-polystyrene (SEBS, G1657), with a polystyrene content of 13% was sourced from Kraton Polymers. Poly(3-hexylthiophene-2,5-diyl) (P3HT), dichloromethane (99.5%), toluene (99.8%), and *m*-xylene (> 99%) were purchased from Sigma-Aldrich. Silver nanowires (AgNWs, 1.0 wt%; average diameter, 75–105 nm; length, 60–100 μm) with isopropyl alcohol (IPA) were purchased from Kechuang. PDMS (Sylgard 184 silicone elastomer kit) was purchased from Dow Corning. Commercial granulated white sugar was purchased from CJ CheilJedang. Ecoflex 00-30 and a silicone pigment (Silc Pig, Pantone 488 C) was purchased from Smooth-On Inc.

Formation of irreproducible SEBS wrinkle

The fabrication of the irreproducible SEBS wrinkles involved preparing a SEBS film. First, SEBS was dissolved in *m*-xylene (300 mg/mL) at 150 °C, followed by cooling down to room temperature. Next, a pigment was added (3 wt%) to the SEBS solution to make it opaque and prevent any interference from the sensors in the artificial fingerprint during image scanning. Subsequently, the solution was degassed for 5 min at room temperature in a vacuum chamber to remove any trapped air. Next, the SEBS solution was spin-coated onto glass at 400 rpm for 1 min, followed by drying at room temperature for 8 h to form a solid film. The surface of the SEBS film was treated with UV-O_3 for 20 min using a UV-O_3 cleaner (UVC-150; Omniscience), which features a wavelength of 254 nm and an intensity of 20 mW/cm^2. Toluene was applied to the treated films for 5 s before it was spun at 800 rpm for 30 s. Finally, the SEBS film was dried at room temperature for 2 h.

Fabrication of soft temperature sensor

The fabrication of the soft temperature sensor began with the preparation of a soft electrode based on AgNWs and SEBS. To prepare the AgNWs/SEBS electrode, AgNWs were patterned on glass using a PI tape-based shadow mask produced using a programmable cutting machine (Silhouette Portrait 3). A solution of AgNWs (0.5 wt %, IPA) was drop casted onto the pattern-masked glass and dried at 70 °C. Subsequently, the pattern was thermally welded at 200 °C for 30 min to enhance its electrical conductivity. Next, the SEBS solution was poured over the pattern and allowed to dry at room temperature for 8 h. A P3HT solution was prepared by dissolving P3HT in dichloromethane (1.5 mg/mL) at 70 °C for 30 min. This solution was cooled down to − 20 °C to facilitate the formation of P3HT-NFs through effective π-π interaction with the polythiophene backbone. Thereafter, a diluted PDMS solution (10:1 weight ratio of the base and curing agent) in dichloromethane was blended with the P3HT-NFs solution at a weight ratio of 4:1. This P3HT-NFs/PDMS solution was then dropped onto the prepared AgNWs/SEBS electrode and heated at 110 °C for 20 min. Finally, the device was encapsulated with a thin layer of PDMS (10:1 weight ratio of the base and curing agent) via spin coating at 4000 rpm for 1 min, followed by solidification at 60 °C for 30 min.

Fabrication of soft pressure sensor

The soft pressure sensor was fabricated by preparing a porous PDMS-based pressure-sensing layer and an AgNWs/PDMS-based soft electrode in a vertically stacked configuration. The preparation of the porous PDMS started with mixing granulated sugar and deionized water at a weight ratio of 16:1. The mixture was poured into a mold, manually compressed using a flat object, and covered with weighing paper to prevent cracking during pressure removal. To maintain a constant thickness of the sugar template, excess sugar was removed by doctor blading, followed by drying the sugar template at room temperature for 10 h. Subsequently, the liquid phase PDMS (15:1 weight ratio of the base to curing agent) was infiltrated into the sugar template for 30 min to ensure adequate infiltration, followed by curing at 60 °C for 4 h. Finally, the sample was immersed in water at 110 °C for 1 h to dissolve the sugar template. The porous PDMS was rinsed with water, dried, and diced into 5 × 5 mm^2 dimensions.

Soft AgNWs/PDMS electrodes were fabricated by following the same steps as described above for AgNWs/SEBS, but using PDMS instead of SEBS. The liquid PDMS (10:1 weight ratio of the base and curing agent) was degassed and spin-coated at 400 rpm for 60 s onto the patterned AgNWs, followed by curing in an oven at 100 °C for 1 h. The pressure sensor was constructed fabricated by integrating AgNWs/PDMS electrodes with the porous PDMS. PDMS (20:1 weight ratio of the base and curing agent) was used as an adhesive layer to bond the porous PDMS and AgNWs/PDMS electrodes. The ratio of 20:1 was optimal for the adhesive layer to prevent a significant impact of the applied pressure. The diced porous PDMS was vertically assembled between the two soft electrodes and subsequently cured in an oven at 60 °C for 2 h.

Fabrication of soft bimodal sensor and artificial finger pad

The soft bimodal sensor was fabricated with a vertical assembly of soft temperature and pressure sensors. To ensure robust integration, PDMS (20:1 weight ratio of the base to curing agent) was used as the adhesive layer between two soft sensors. PDMS, spin-coated at 4000 rpm for 30 s between the two sensors, was fully cured in an oven at 60 °C for 2 h. The artificial finger pad was fabricated by vertically stacking the soft temperature sensor equipped with an artificial fingerprint and the soft pressure sensor. The fabrication process was slightly different from that of the temperature sensor; the artificial fingerprint was formed after preparing the AgNWs/SEBS electrode. Subsequently, the temperature sensor was fabricated as described earlier. The fabricated temperature sensor with the artificial fingerprint was integrated with the soft pressure sensor using the same procedure as that used for the soft bimodal sensor.

Fabrication of identifiable adaptive soft robot

The pneumatically actuatable soft robots were fabricated using molds created with a 3D printer. A mixture of Ecoflex 00-30, with a 1:1 weight ratio of parts A and B, was poured into the mold and degassed in a

vacuum chamber. The mixture was then cured at 60 °C for 2 h. After curing, the robot body was sealed with Ecoflex 00-30 and connected to an air tube that regulated air pressure via the control system. Spiky legs were attached to the head and tail of the robot. An identifiable artificial finger pad electronics system, incorporating a temperature sensor, was integrated into the robot's head and interfaced with the control system.

Characterizations of arbitrary patterns and devices

The morphologies of artificial fingerprints were assessed using several characterization techniques. An optical microscope (Olympus, BX53M), a portable microscope (AM4113ZT, Dino-lite Korea), a scanning electron microscope (SEM, Nano230, Nova Ltd.), and an atomic force microscope (AFM, NX-10, Park Systems Inc.) in the tapping mode were used for this purpose. Three-dimensional imaging, amplitude, and height were characterized using a confocal laser scanning microscope (OLS3100, Olympus). An FT-IR spectrometer (Spectrum Two, Perkin Elmer) equipped with an attenuated total reflectance accessory was used to obtain the spectra of SEBS under varying durations of the UV-O_3 treatment. The molecular weight of SEBS before and after UV-O_3 treatment was analyzed by GPC (miniDAWN TREOS, Wyatt). Mechanical properties such as stress-strain curves and pressure measurements of the devices were obtained using a force gauge (M7-50, Mark-10 Corp.). The capacitance changes in the pressure sensor were tracked using an LCR meter (E4980A, Keysight Technology, Inc.). Temperature was measured using a digital thermometer (Fluke 568) equipped with a K-type thermocouple probe. The resistance changes in the temperature sensor were measured using a precision source/measurement unit (B2912B, Keysight Technologies, Inc.). The temperature maps during object gripping were captured using an infrared camera (FLIR ONE Pro; FLIR Systems). Finally, the images of the artificial fingerprints were acquired using a commercially available fingerprint scanner (Arduino JB-101B).

Data availability

The source data underlying all plots within this paper are provided as a Source Data file. Additional data that supports the findings of this study are available from the corresponding author upon request.

Code availability

The codes utilized in this study are provided in the Supplementary Information file. Additional codes used in this study are available on Zenodo (https://zenodo.org/records/14742359).

References

1. Kim, J. B. et al. Wrinkles and deep folds as photonic structures in photovoltaics. *Nat. Photonics* **6**, 327–332 (2012).
2. Liu, Y., Feng, Z., Xu, C., Chatterjee, A. & Gorodetsky, A. A. Reconfigurable Micro- and Nano-Structured Camouflage Surfaces Inspired by Cephalopods. *ACS Nano* **15**, 17299–17309 (2021).
3. Wang, Y. et al. Controlling silk fibroin conformation for dynamic, responsive, multifunctional, micropatterned surfaces. *Proc. Natl. Acad. Sci. USA* **116**, 21361–21368 (2019).
4. Zeng, S. et al. Dynamic multifunctional devices enabled by ultrathin metal nanocoatings with optical/photothermal and morphological versatility. *Proc. Natl. Acad. Sci. USA* **119**, e2118991119 (2022).
5. Chen, T.-L. et al. Fabrication of frog-skin-inspired slippery antibiofouling coatings through degradable block copolymer wrinkling. *Adv. Funct. Mater.* **31**, 2104173 (2021).
6. Zhang, Z., Zhang, T., Zhang, Y. W., Kim, K.-S. & Gao, H. Strain-controlled switching of hierarchically wrinkled surfaces between superhydrophobicity and superhydrophilicity. *Langmuir* **28**, 2753–2760 (2012).
7. Chan, E. P., Smith, E. J., Hayward, R. C. & Crosby, A. J. Surface wrinkles for smart adhesion. *Adv. Mater.* **20**, 711–716 (2008).
8. Jeong, H. E., Kwak, M. K. & Suh, K. Y. Stretchable, adhesion-tunable dry adhesive by surface wrinkling. *Langmuir* **26**, 2223–2226 (2010).
9. Lee, G., Zarei, M., Wei, Q., Zhu, Y. & Lee, S. G. Surface wrinkling for flexible and stretchable sensors. *Small* **18**, e2203491 (2022).
10. Xie, M. et al. Pattern memory surface (PMS) with dynamic wrinkles for unclonable anticounterfeiting. *ACS Mater. Lett.* **1**, 77–82 (2019).
11. Bae, H. J. et al. Biomimetic microfingerprints for anti-counterfeiting strategies. *Adv. Mater.* **27**, 2083–2089 (2015).
12. Kim, K. et al. High-definition optophysical image construction using mosaics of pixelated wrinkles. *Adv. Sci.* **7**, 2002134 (2020).
13. Ma, T. et al. Dynamic wrinkling pattern exhibiting tunable fluorescence for anticounterfeiting applications. *Nat. Commun.* **11**, 1811 (2020).
14. Hou, H., Yin, J. & Jiang, X. Smart patterned surface with dynamic wrinkles. *Acc. Chem. Res.* **52**, 1025–1035 (2019).
15. Kwiatkowska, M., Franklin, S. E., Hendriks, C. P. & Kwiatkowski, K. Friction and deformation behaviour of human skin. *Wear* **267**, 1264–1273 (2009).
16. Nachman, M. & Franklin, S. E. Artificial Skin Model simulating dry and moist in vivo human skin friction and deformation behaviour. *Tribol. Int.* **97**, 431–439 (2016).
17. Lee, G. et al. Fingerpad-inspired multimodal electronic skin for material discrimination and texture recognition. *Adv. Sci.* **8**, 2002606 (2021).
18. Qiao, H., Sun, S. & Wu, P. Non-equilibrium-growing aesthetic ionic skin for fingertip-like strain-undisturbed tactile sensation and texture recognition. *Adv. Mater.* **35**, 2300593 (2023).
19. Park, J., Kim, M., Lee, Y., Lee, H. S. & Ko, H. Fingertip skin–inspired microstructured ferroelectric skins discriminate static/dynamic pressure and temperature stimuli. *Sci. Adv.* **1**, e1500661 (2015).
20. Kang, H. et al. Fingerprint-inspired conducting hierarchical wrinkles for energy-harvesting E-skin. *Adv. Funct. Mater.* **29**, 1903580 (2019).
21. Qiu, Y. et al. Nondestructive identification of softness via bioinspired multisensory electronic skins integrated on a robotic hand. *Npj Flex. Electron.* **6**, 45 (2022).
22. Tran, H., Feig, V. R., Liu, K., Zheng, Y. & Bao, Z. Polymer chemistries underpinning materials for skin-inspired electronics. *Macromolecules* **52**, 3965–3974 (2019).
23. Shen, Z. & Feng, J. Mass-produced SEBS/graphite nanoplatelet composites with a segregated structure for highly stretchable and recyclable strain sensors. *J. Mater. Chem. C* **7**, 9423–9429 (2019).
24. Gama, N., Ferreira, A., Evtuguin, D. & Barros-Timmons, A. Modified cork/SEBS composites for 3D printed elastomers. *Polym. Adv. Technol.* **33**, 1881–1891 (2022).
25. Rojas-Quintero, J. A. & Rodríguez-Liñán, M. C. A literature review of sensor heads for humanoid robots. *Robot. Auton. Syst.* **143**, 103834 (2021).
26. Ajibo, C. A., Ishi, C. T., Mikata, R., Liu, C. & Ishiguro, H. Analysis of body gestures in anger expression and evaluation in android robot. *Adv. Robot.* **34**, 1581–1590 (2020).
27. Asano, Y., Okada, K. & Inaba, M. Design principles of a human mimetic humanoid: Humanoid platform to study human intelligence and internal body system. *Sci. Robot.* **2**, eaaq0899 (2017).
28. Billard, A. & Kragic, D. Trends and challenges in robot manipulation. *Science* **364**, eaat8414 (2019).
29. Hughes, J. A. E., Maiolino, P. & Iida, F. An anthropomorphic soft skeleton hand exploiting conditional models for piano playing. *Sci. Robot.* **3**, eaau3098 (2018).
30. Qu, X. et al. Artificial tactile perception smart finger for material identification based on triboelectric sensing. *Sci. Adv.* **8**, eabq2521 (2022).
31. Liu, F. et al. Neuro-inspired electronic skin for robots. *Sci. Robot.* **7**, eabl7344 (2022).
32. Sim, K. et al. Metal oxide semiconductor nanomembrane–based soft unnoticeable multifunctional electronics for wearable human-machine interfaces. *Sci. Adv.* **5**, eaav9653 (2019).

33. Allen, N. S. et al. Degradation and stabilisation of styrene–ethylene–butadiene–styrene (SEBS) block copolymer. *Polym. Degrad. Stab.* **71**, 113–122 (2000).
34. Luengo, C. et al. Photo-oxidative degradation mechanisms in styrene–ethylene–butadiene–styrene (SEBS) triblock copolymer. *Polym. Degrad. Stab.* **91**, 947–956 (2006).
35. Allen, N. S. et al. Photooxidation of styrene–ethylene–butadiene–styrene (SEBS) block copolymer. *J. Photochem. Photobiol. A* **162**, 41–51 (2004).
36. Rabek, J. F. *Photodegradation of Polymers: Physical Characteristics and Applications* 109–135 (Springer, Berlin, Heidelberg, 1996).
37. Chen, X. & Hutchinson, J. W. Herringbone buckling patterns of compressed thin films on compliant substrates. *J. Appl. Mech.* **71**, 597–603 (2004).
38. Fukuda, T., Dario, P. & Yang, G.-Z. Humanoid robotics-History, current state of the art, and challenges. *Sci. Robot.* **2**, eaar4043 (2017).
39. Belpaeme, T., Kennedy, J., Ramachandran, A., Scassellati, B. & Tanaka, F. Social robots for education: A review. *Sci. Robot.* **3**, eaat5954 (2018).
40. Choi, Y., Choi, M., Oh, M. & Kim, S. Service robots in hotels: understanding the service quality perceptions of human-robot interaction. *J. Hosp. Mark. Manag.* **29**, 613–635 (2020).
41. Vasconez, J. P., Kantor, G. A. & Auat Cheein, F. A. Human–robot interaction in agriculture: A survey and current challenges. *Biosyst. Eng.* **179**, 35–48 (2019).
42. Di Nuovo, A. & McClelland, J. L. Developing the knowledge of number digits in a child-like robot. *Nat. Mach. Intell.* **1**, 594–605 (2019).
43. Yang, G.-Z. Robot learning-Beyond imitation. *Sci. Robot.* **4**, eaaw3520 (2019).
44. Oprişan, C. et al. Experimental determination of the Young's modulus for the fingers with application in prehension systems for small cylindrical objects. *IOP Conf. Ser. Mater. Sci. Eng.* **147**, 012058 (2016).
45. Ying, W. B. et al. Waterproof, highly tough, and fast self-healing polyurethane for durable electronic skin. *ACS Appl. Mater. Interfaces* **12**, 11072–11083 (2020).
46. Lee, Y. et al. Standalone real-time health monitoring patch based on a stretchable organic optoelectronic system. *Sci. Adv.* **7**, eabg9180 (2021).
47. Kim, H.-J., Sim, K., Thukral, A. & Yu, C. Rubbery electronics and sensors from intrinsically stretchable elastomeric composites of semiconductors and conductors. *Sci. Adv.* **3**, e1701114 (2017).
48. Guan, Y.-S. et al. Air/water interfacial assembled rubbery semiconducting nanofilm for fully rubbery integrated electronics. *Sci. Adv.* **6**, eabb3656 (2020).
49. Xu, F. & Zhu, Y. Highly conductive and stretchable silver nanowire conductors. *Adv. Mater.* **24**, 5117–5122 (2012).
50. Li, Q., Duan, T., Shao, J. & Yu, H. Fabrication method for structured porous polydimethylsiloxane (PDMS). *J. Mater. Sci.* **53**, 11873–11882 (2018).
51. Masihi, S. et al. Highly sensitive porous PDMS-based capacitive pressure sensors fabricated on fabric platform for wearable applications. *ACS Sens.* **6**, 938–949 (2021).
52. Kherroub, D. E. & Boulaouche, T. Maghnite: novel inorganic reinforcement for single-step synthesis of PDMS nanocomposites with improved thermal, mechanical and textural properties. *Res. Chem. Intermed.* **46**, 5199–5217 (2020).
53. Liu, X. et al. New non-invasive techniques to quantify skin surface strain and sub-surface layer deformation of finger-pad during sliding. *Biotribology* **12**, 52–58 (2017).
54. Ruth, S. R. A. & Bao, Z. Designing tunable capacitive pressure sensors based on material properties and microstructure geometry. *ACS Appl. Mater. Interfaces* **12**, 58301–58316 (2020).
55. Li, R. et al. Research progress of flexible capacitive pressure sensor for sensitivity enhancement approaches. *Sens. Actuator A Phys.* **321**, 112425 (2021).
56. Zhang, Z. et al. Highly transparent, self-healable, and adhesive organogels for bio-inspired intelligent ionic skins. *ACS Appl. Mater. Interfaces* **12**, 15657–15666 (2020).
57. Zhang, Z., Yu, Y., Yu, H., Feng, Y. & Feng, W. Water-resistant conductive organogels with sensation and actuation functions for artificial neuro-sensory muscular systems. *SmartMat* **3**, 632–643 (2022).
58. Yu, Y. et al. Carbon dots-based ultrastretchable and conductive hydrogels for high-performance tactile sensors and self-powered electronic skin. *Small* **19**, 2204365 (2022).
59. Fraser, K. C. et al. Tracking the conservation promise of movement ecology. *Front. Ecol. Evol.* **6**, 150 (2018).
60. Katzner, T. E. & Arlettaz, R. Evaluating contributions of recent tracking-based animal movement ecology to conservation management. *Front. Ecol. Evol.* **7**, 519 (2020).
61. Hays, G. C. et al. Translating marine animal tracking data into conservation policy and management. *Trends Ecol. Evol.* **34**, 459–473 (2019).
62. Wang, R., Han, L., Wu, C., Dong, Y. & Zhao, X. Localizable, identifiable, and perceptive untethered light-driven soft crawling robot. *ACS Appl. Mater. Interfaces* **14**, 6138–6147 (2022).

Acknowledgements

This work was supported by the UBSI Research Fund (1.230067.01) of UNIST (Ulsan National Institute of Science & Technology) and the National Research Foundation of Korea (NRF) grants funded by the Korean government (NRF–2021R1C1C1007714 and RS-2024-00346943). Z.L. acknowledges the support from presidential frontier faculty fellow funding and high-priority area research seed grant from the University of Houston. We thank Euna Kim and Inwoo Lee for their experimental support.

Author contributions

J.L. and K.S. conceived the concept and designed the experiments. J.L. and H.P. prepared materials, fabricated devices, and characterized device performance. H.P. and S.K. performed analysis of materials. Z.L. and C.L. performed numerical analysis. J.L., H.P., and K.S. analyzed the experimental data and wrote the manuscript. All authors reviewed and revised the manuscript.

Competing interests

The authors declare no competing interests.

Additional information

Supplementary information The online version contains supplementary material available at https://doi.org/10.1038/s41467-025-57498-y.

Correspondence and requests for materials should be addressed to Kyoseung Sim.

Peer review information *Nature Communications* thanks Wei Feng, Qijun Sun, and the other anonymous reviewer(s) for their contribution to the peer review of this work. A peer review file is available.